

# Development of Lightweight Oil Catch Tank Produced by Laser Powder Bed Fusion

Keita Watanabe Hiroataka Kurita Shinya Iwasaki Riku Mitsui Takashi Nagao  
Tsuchiharu Tashiro Makoto Ichimura Yoshiaki Kano Jun Kusui

当論文は、SAE 2023-01-1807/JSAE 20239507として、SETC2023 (Small Powertrains and Energy Systems Technology Conference)にて発表され、優秀論文6選に選出されたものです。

Reprinted with permission Copyright © 2023 SAE INTERNATIONAL and Copyright © 2023 SAE Japan (Further use or distribution is not permitted without permission from SAE)

## 要旨

3Dプリンターとも呼ばれる三次元積層造形法は、従来工法では実現困難な複雑形状を具現化するだけでなく、多品種少量生産への適正が高く、また開発および生産におけるリードタイム短縮などにも寄与する革新的な工法として注目を集めている。その中でも、金属材料の三次元積層造形法の一つであるレーザーパウダーベッドフュージョン(L-PBF)は、精巧な造形性に加え優れた材料特性を発現することから、航空宇宙産業を中心に実用化が進んでいる。本報では、L-PBF法を活用し、輸送機器に広く用いられているオイルキャッチタンクの軽量化に取り組んだ。積層造形条件の最適化、材料の冶金的および機械的特性の把握、更にはL-PBFの形状自由度を反映した設計により、従来比60%の劇的な軽量化に成功した。

## Abstract

Laser powder bed fusion is one of the metal additive manufacturing technologies, so-called 3D printing. It has attracted great attentions due to high geometrical flexibility and remarkable metallurgical characteristics. An oil catch tank has been widely used in automotive industries for filtering oil vapors or carbon sludge from blow-by gas as a conventional usage. A pneumatic valve system mainly adopted to high-performance engines is also a potential application of it because undesirable oil infiltrates into air springs during engine operation, resulting in an excess spring pressure. This work focused on developing a lightweight oil catch tank which can be applied to a pneumatic valve system by taking advantage of additive manufacturing techniques. Al-Mg-Sc alloy powder with high tensile strength as well as high ductility were used under the consideration of specific strength, printability and availability. Test specimens fabricated with optimal printing parameters exhibited mechanical properties comparable to a high-strength wrought material as well as unique metallurgical characteristics due to rapid solidification. The newly developed oil catch tank was designed taking into account material properties acquired in this study and functional requirements of the component. The developed tank had a monolithic structure whereas conventional one consists of multiple parts. Moreover, the wall thickness was minimized from location to location based on the induced stress distribution. These are distinct geometrical features which are very difficult to be created by classical processes. As a result, the novel 3D-printed tank in this work was around 60% lighter than conventional one, and experimentally demonstrated to meet the functional requirements.

## 1

## INTRODUCTION

Oil catch tanks have been widely used in automotive industries to separate gas and other substances such as oil. They basically consist of a vessel, an inlet, an outlet, and a drain as illustrated in Figure 1. Gas including impurities

flows into and out of the vessel through the inlet and the outlet respectively, resulting in separation due to a difference of specific weight. It is typically installed into a ventilation circuit of blow-by gas to filter oil vapors or carbon sludge<sup>[1]</sup>. Another is placed in a transmission case of a hybrid vehicle to collect automatic transmission fluid

and distribute it to a motor for cooling<sup>[2]</sup>. A pneumatic valve system (PVS) often adopted in high-performance engines is also a potential application of an oil catch tank. The system employs compressed air springs instead of conventional coil springs as shown in Figure 2(a) and play a key role to precisely drive both intake and exhaust valves even in extremely high revolution. During engine operation, lubricant oil surrounding the system gradually infiltrates into the air springs, leading to unwanted increase in pressure. Figure 2(b) shows the conceptual design of a ventilation circuit for a PVS in which compression air is regularly vented out from the springs and flows into the oil catch tank through the gallery installed in the cylinder head. In this case, the oil catch tank is required to withstand high pressure equivalent to or greater than that of the air springs. In addition, the temperature of the tank is expected to reach up to 150°C due to heat generated from the engine because the tank is supposed to be mounted closed to the engine. It also can be said that the lighter, the better for high-performance engines. For these reasons, the oil catch tank compatible to a PVS should achieve both lightness and durability.

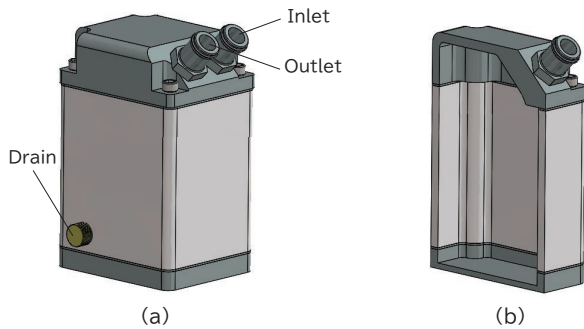


Fig. 1 Schematically illustrated (a) appearance and (b) cross-sectional view of general oil catch tank

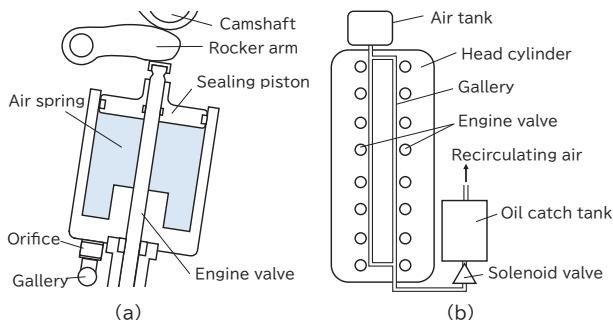


Fig. 2 Schematic illustration of (a) cross-sectional view of PVS and (b) ventilation circuit concept

Additive manufacturing technologies, also called as 3D printing, have been gradually put to practical applications in various industries such as medical, aerospace, aviation and automotive. As explained in more detail later, they are characterized by a layer-by-layer process which can offer high design flexibility. This work aims to develop a lightweight oil catch tank that can be applied to a PVS by means of an additive manufacturing technique.

## 2 EXPERIMENTAL

### 2-1. Laser powder bed fusion

Laser powder bed fusion (L-PBF) is one of the most widely used metal additive manufacturing technologies. In a L-PBF process, a thin layer of powder is distributed across a building platform and selectively melted by a high-power laser according to two-dimensionally sliced data of a product, and this sequence is repeated until a three-dimensional structure is completely built. This unique layer-by-layer technique offers design flexibility with a high resolution<sup>[3][4]</sup>. During the L-PBF process, the laser irradiation spot is very small and moves around so rapidly that the melted material experiences immediate solidification with a high cooling rate. Tang et al. estimated the cooling rate of the L-PBF process is approximately  $2 \times 10^6$  K/sec in AlSi10Mg alloy<sup>[5]</sup>, which is extremely faster than conventional casting processes with cooling rate of 100 K/sec at most<sup>[6]</sup>. The rapid solidification and high cooling rate serve to create very fine microstructures accompanying with remarkable metallurgical characteristics demonstrated in the various materials<sup>[7][8][9]</sup>. Nowadays, it has also attracted a lot of interests from the viewpoint of carbon neutrality<sup>[10]</sup>. Figure 3 shows a schematic illustration of the L-PBF process and its key parameters. In the L-PBF process, volumetric energy density  $E_d$  (J/mm<sup>3</sup>) calculated by the following equation has been often utilized to explore optimal process parameters<sup>[11]</sup>.

$$E_d = \frac{P}{v \cdot S \cdot t} \quad (1)$$

where  $P$  is the laser power (W),  $v$  is the laser scanning speed (mm/sec),  $S$  is the hatch spacing (mm) between the adjacent tracks, and  $t$  is the powder layer thickness (mm).

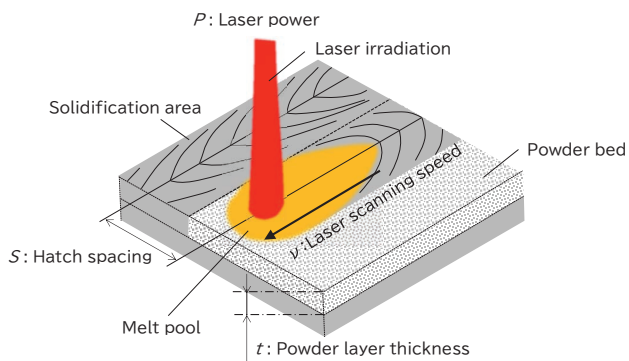


Fig. 3 Schematic illustration of L-PBF process and key parameters

## 2-2. Al-Mg-Sc alloy

Strength-to-weight ratio is of importance in the material selection for weight reduction. From this perspective, both Al alloys and Ti alloys can be potential materials since they have a great strength-to-weight ratio and are available in the L-PBF technology. However, if a Ti alloy is used, design features such as a wall thickness and a strut are required to be much finer than those in case of Al alloys to achieve the same weight because the density of Ti alloys is around 60% greater than Al alloys. Extremely fine features could make printing more difficult and, in severe cases, lead to a deformation or a collapse. Additionally, Ti alloys often exhibit a martensitic transformation accompanying with a rapid volume change, which could also increase a risk of deformation. For these reasons, one of the high-strength Al alloys available in the L-PBF process, an Al-Mg-Sc alloy was adopted in this work. The effects of Sc addition to conventional casting Al alloys have been widely investigated<sup>[12][13]</sup>. In the solidification process of Al alloys including Sc,  $\text{Al}_3\text{Sc}$  intermetallic particles preliminarily precipitate in the molten alloy before the  $\alpha$ -Al phase forms.  $\text{Al}_3\text{Sc}$  has  $\text{L}_{12}$  lattice structure, which is a fcc-based structure, and it was reported the lattice misfit between the  $\alpha$ -Al matrix and  $\text{Al}_3\text{Sc}$  is considerably small, approximately 1.3%<sup>[14]</sup>. Due to the high coherence with the matrix,  $\text{Al}_3\text{Sc}$  can disperse homogeneously with high density and subsequently act as a nucleation site for the  $\alpha$ -Al phase to solidify, resulting in a remarkable grain refinement. Furthermore, the homogeneously dispersed  $\text{Al}_3\text{Sc}$  precipitates serve to inhibit dislocations from

moving. Hence, the alloys exert a great precipitation strengthening effect as well as recrystallization suppression up to a certain elevated temperature. Several researchers have investigated Al-Mg-Sc alloys fabricated by the L-PBF process. A.B. Spierings et al. conducted comprehensive studies related to the microstructural features and suggested that  $\text{Al}_3\text{Sc}$  particles contribute grain refinement in the additively manufactured Al-Mg-Sc alloy as well<sup>[15][16]</sup>. Kimura et al. studied aging behaviors of this alloy and found that the hardness is not likely to be susceptible to the aging condition if the temperature ranges from 300°C to 350°C and holding time is more than 4 hours<sup>[17]</sup>. 325°C for 4 hours is proposed as the peak aging condition in their work. Shi et al. evaluated effects of the building platform temperature and the building orientation on the mechanical properties of an Al-Mg-Sc alloy containing small amount of Cu<sup>[18]</sup>. It was reported that both affect the as-fabricated mechanical properties, however, all the specimens built with the different condition exhibit almost the same tensile properties after the aging treatment. That is to say, the aging treatment can give this alloy consistent tensile properties.

## 2-3. Investigation on metallurgical characteristic

Metallurgical characteristics of the Al-Mg-Sc alloy were firstly investigated. Centrifugal-atomized powder whose chemical composition is shown in Table 1 was used. The cumulative distribution of the particle size showed 28.6 $\mu\text{m}$  for  $d_{10}$ , 43.4 $\mu\text{m}$  for  $d_{50}$  and 65.0 $\mu\text{m}$  for  $d_{90}$ . One of the L-PBF printer, LUMEX Avance-25, were employed. Laser power, laser scanning speed, hatch spacing and layer thickness were 340W, 900mm/sec, 0.1mm and 0.04mm respectively. The volumetric energy density  $E_d$  is calculated as 94.4J/mm<sup>3</sup> based on the equation (1). The above optimal parameters to create a fully dense specimen were established through the preliminary experiment. In the experiment, 35 × 8 × 15mm cuboid specimens were fabricated with varying laser power, laser scanning speed and hatch spacing. The fabricated specimens went through a density measurement by Archimedes method. Figure 4 shows the relationship between the density of the specimen and the volumetric energy density. The density of the specimen increases as

the volumetric energy density increases. At volumetric energy densities above  $80\text{J}/\text{mm}^3$ , the specimen densities reach up to around  $2.67\text{g}/\text{cm}^3$  which is the theoretical density of the material. The data point in red corresponds to the condition used in this work as the optimal parameters described above. The cross-sectional view of the cuboid specimen printed with the optimal parameters is shown in Figure 5 where no evident defects can be observed.

Table 1 Chemical composition of powder material

							mass%
Mg	Sc	Zr	Mn	Si	Fe	Al	
4.90	0.78	0.29	0.41	0.06	0.17	Bal.	

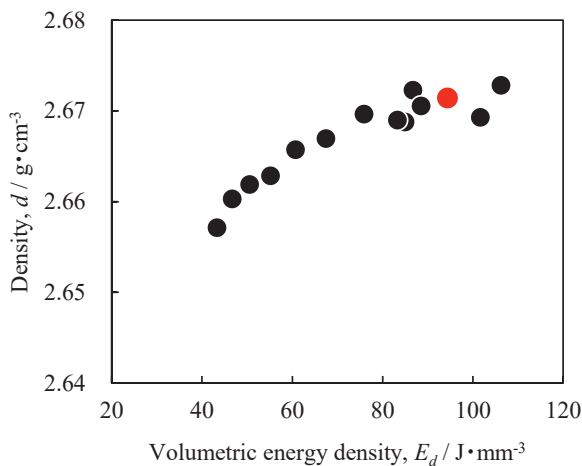


Fig. 4 Relationship between specimen density and volumetric energy density



Fig. 5 Cross-sectional view of specimen fabricated with optimal parameters

Sheet-shaped specimens with the dimension of  $23 \times 119 \times 4\text{mm}$  referred to as specimen A,  $33 \times 95 \times 4\text{mm}$  referred to as specimen B were produced. Specimen A was fabricated with the orientation where the longitudinal direction was aligned with the stacking direction (Vertical direction). A part of specimen B was produced with the same orientation as specimen A. Additionally, specimen B was built with the orientation at  $45^\circ$  to the building platform as described in Figure 6. The building platform was kept at  $40^\circ\text{C}$  during the fabrication. The produced specimens were aged at  $325^\circ\text{C}$  for 4 hours followed by air cooling. Surface roughness was evaluated using optical 3D surface profilometer, KEYENCE VR-3000. For the microstructure observation, specimen A was grounded and polished followed by etching in Keller's reagent. Microstructures were analyzed by an optical microscopy, a scanning electron microscope (SEM) and a transmission electron microscope (TEM). Electron backscatter diffractions (EBSD) were obtained with a step size of  $0.5\mu\text{m}$  using JEOL JSM-6490A with TSL-OIM device. The specimen surfaces went through ion milling using JEOL SM-09010 before the EBSD analysis. A grain boundary was defined if the misorientation between two points was greater than  $15^\circ$ . Thermo Scientific Talos F200X operated at  $200\text{kV}$  was used for TEM observation. A thin foil specimen for TEM observation was prepared using JEOL EM-09100IS ion milling. Bright field (BF) images were captured in scanning transmission electron microscopy (STEM) mode. Energy dispersive X-ray spectroscopy (EDS) analyses were also conducted. AVK-A Vickers hardness tester was used to evaluate the hardness at ambient temperature on five (5) points for one of test specimen A and the average was calculated. The load and the loading time were  $5\text{kgf}$  and  $15\text{sec}$  respectively. Specimen A and B were processed into the tensile test coupons and the fatigue test coupons respectively as described in Figure 7. All the surfaces in the tensile test coupons were finished by machining. In case of the fatigue test coupons, only the contour and the holes were machined, which means most of the surface remained in the as-built state. Tensile tests at ambient temperature were carried out using an universal tester, AG-100kN IS with the tensile speed of  $0.13\text{mm}/\text{min}$  up to

the yield strength, and afterward 2.5mm/min. Tensile tests at 150°C were conducted using an universal testing machine, AG-100kNXplus with the strain rate of 0.42%/min up to the yield strength, and afterward 8.4%/min. Averages of the tensile properties were calculated from 18 measurements. Fatigue properties at 150°C were examined using a bending fatigue tester with the stress ratio (Minimum stress divided maximum stress) of -1 and the frequency of 25Hz.

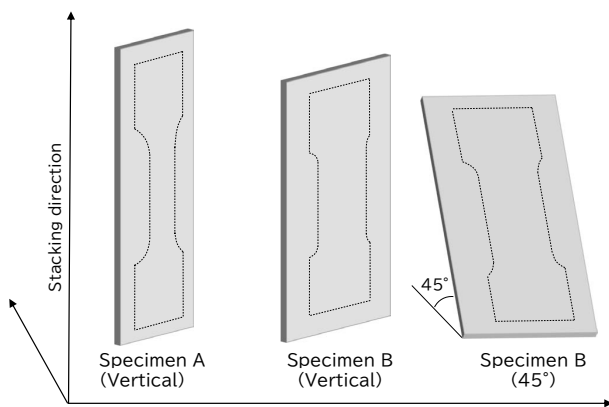


Fig. 6 Schematic drawing of fabricated specimen

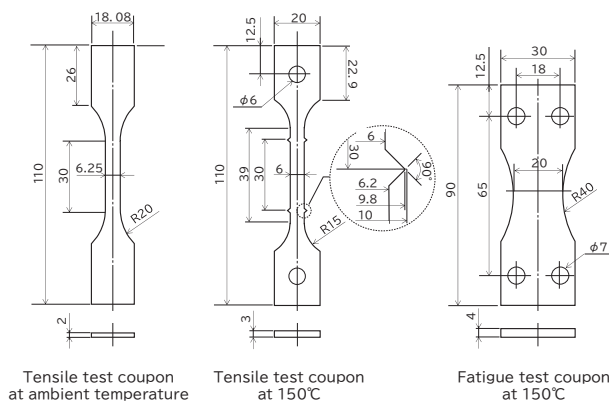


Fig. 7 Test coupon geometry for mechanical property test

### 3 RESULT AND DISCUSSION

#### 3-1. Microstructural characterization

Figure 8 shows a microstructure along the stacking direction. There are no noticeable defects such as a lack of fusion or a keyhole. The relative density of this specimen evaluated by an image analysis was 99.9%. It can be considered fully dense owing to the optimized printing parameters. The microstructure comprises full of

semi-circular microstructures with the width of around 200µm. The profile of the melt pool track during the laser irradiation is evident. One semi-circular track is overlapping with the adjacent, underneath and upper tracks, which implies the material experienced multiple melting and solidification. In addition, the heat that dissipated from a melt pool to a solidified material could cause an intrinsic heat treatment. It was reported this treatment encourages precipitations in age-hardening alloys including the Al-Mg-Sc alloy<sup>[19]</sup>.

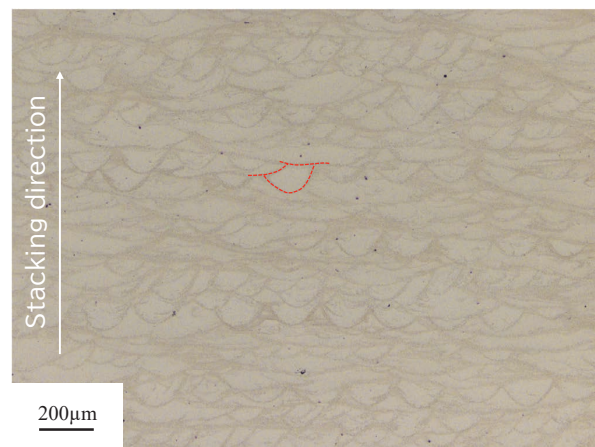


Fig. 8 Optical micrograph (Area enclosed by red dotted line describes single melt pool)

Two regions of different grain sizes are clearly distinguishable in the EBSD analysis results as shown in Figure 9. Very fine equiaxed grains are formed along the melt pool boundaries whereas columnar grains develop from the vicinity of the melt pool boundaries toward the center of the melt pools. The approximate size of the equiaxed grains ranges from 1 to 3µm while that of the columnar grains ranges from 2 to 20µm in the longitudinal direction. It is notable that the observed grains are remarkably finer than those of conventional casting Al alloys whose grain sizes are from several tens to hundreds of micrometers<sup>[20]</sup>. The finer grains potentially lead to the greater yield strength according to the Hall-Petch relation. Additionally, Kimura et al reported the Al-Mg-Sc alloy exhibits the greater volume fraction of the fine equiaxed grains than that of AlSi10Mg, a typical Al alloy for L-PBF<sup>[16]</sup>. Therefore, these refined grains can be one of the strengthening factors for the Al-Mg-Sc alloy. The two distinct regions also exhibit

difference in the grain orientation. The pole figures in Figure 10 displays the columnar grains have a strong texture of <001> direction along the stacking direction, on the contrary, the fine grains show no tendency of such texture. This indicates grains oriented to <001> direction developed from the bottom to the center of the melt pools during solidification, resulting in the columnar grains.

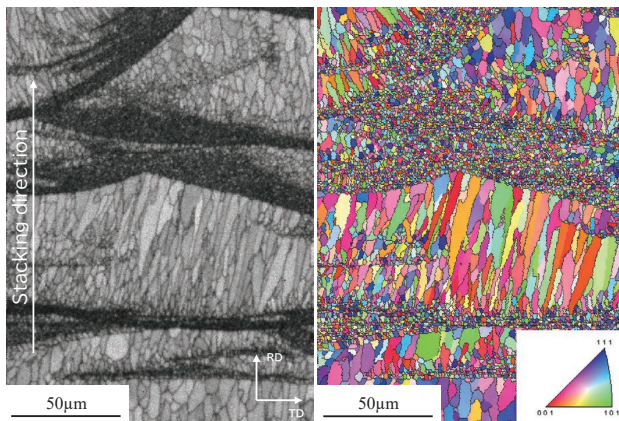


Fig. 9 EBSD inverse pole figure map

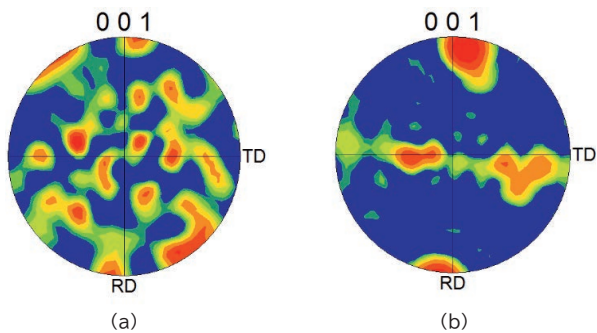


Fig. 10 [001] pole figure of (a) fine grain and (b) columnar grain

EDS mappings of the columnar grain region at low magnification are shown in Figure 11. Fe-Mn rich and Mg-Si rich precipitates are observed within the grain as well as on the grain boundary. The precipitates on the grain boundary appear to be larger than those within the grain itself. Sc is spread throughout but appears to slightly segregate at the grain boundaries. The high magnification mapping in Figure 12 shows an evidence of Sc rich precipitates that are much finer than the other precipitates, with the size of around 5nm. This Sc rich precipitates are considered as  $Al_3Sc$  according to the

previous studies<sup>[14][15][16][17]</sup>. Figure 11 and Figure 12 additionally suggest that Mg still exists as a solute element dissolving into the matrix although a certain amount of Mg is consumed as the precipitates.

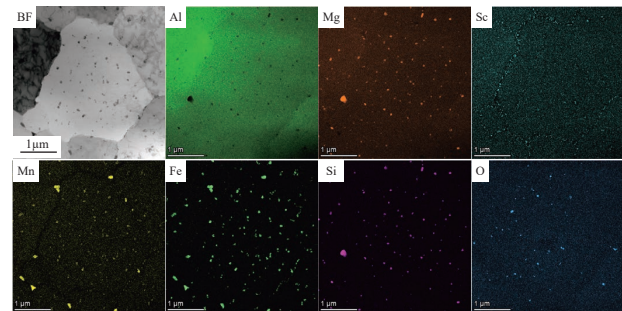


Fig. 11 Low magnification EDS mapping

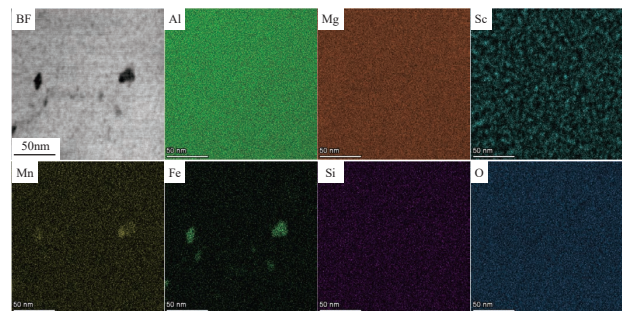


Fig. 12 High magnification EDS mapping

### 3-2. Mechanical characteristic

Table 2 represents the hardness and the mechanical properties at ambient temperature and 150°C obtained in this study. The Al-Mg-Sc alloy fabricated through the L-PBF process exhibited mechanical properties superior to wrought A2024-T6 alloy<sup>[21]</sup>, a typical high-strength Al alloy. Referring to the microstructural features observed in the previous section, this can be attributed to extremely refined grains, precipitation strengthening mainly of  $Al_3Sc$  and solid solution strengthening of Mg. In this work, the printing parameters were determined by evaluating density as an indicator through the preliminary experiment. However, further study is required to elucidate the relationship between mechanical properties, microstructure and printing parameters since they are expected to affect each other.

Table 2 Hardness and tensile characteristic

Test temperature: Ambient					
		Hardness (HV5)	UTS (MPa)	YS (MPa)	EL (%)
Al-Mg-Sc alloy fabricated by L-PBF	Ave.	171.0	526.4	498.5	15.4
	Max.	175	530	504	16.8
	Min.	169	524	488	13.6
Wrought A2024-T6 alloy	—	—	475	395	10
Test temperature: 150°C					
		Hardness (HV5)	UTS (MPa)	YS (MPa)	EL (%)
Al-Mg-Sc alloy fabricated by L-PBF	Ave.	—	344.1	262.6	40.9
	Max.	—	349	273	48
	Min.	—	340	249	37
Wrought A2024-T6 alloy	—	—	310	250	17

The fatigue properties at 150°C are shown in Figure 13. As mentioned earlier, the specimens with the different building orientations to the building platform, vertical or 45°, were evaluated. The fatigue strength of the specimen with 45° orientation was 51MPa and that with vertical orientation was 65MPa. Before the fatigue test, it was expected that the orientation vertical to the building platform would be weaker than 45° orientation because the stress could act to split off the intrinsic laminated structure derived from the layer-by-layer process in case of the vertically orientated specimen. However, the results obtained were the opposite of the expectation. That may be explained by the effect of surface roughness. It is well known, in the L-PBF process, a downfacing surface tends to exhibit a rougher surface compared to a surface vertical to a building platform due to adhesion of un-melted powders and the staircase effect. The previous studies have proven that rougher surface can deteriorate the fatigue properties of additively manufactured AlSi10Mg alloys<sup>[22]</sup>. As a results of surface roughness measurement, the mean roughness Ra of the vertical specimen is 7.8µm whereas that of the downfacing surface in the specimen with 45° orientation is 27.5µm. This difference would have a considerable influence on the fatigue property. Hence, in this study, the fatigue property deterioration can be attributed to the difference in the surface roughness of the material.

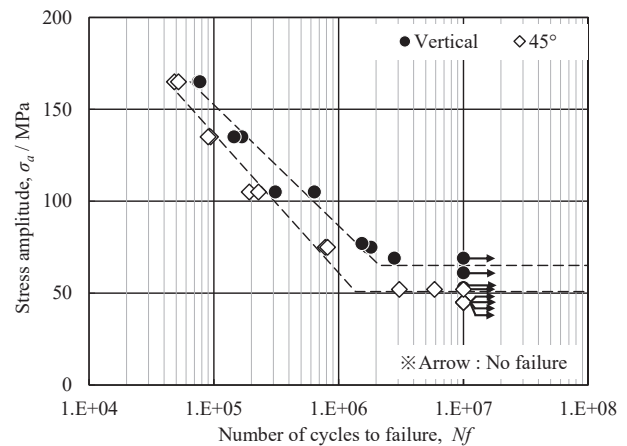


Fig. 13 Fatigue strength

### 3-3. Lightweight design

As the first step in the design process, requirements for the durability and the structure of the component were defined. One of the functional targets was set to be leak-tight and durable at 1.5MPa and 150°C because, as mentioned above, this tank is expected to receive the high-pressure air from a PVS system and be exposed to high temperature up to 150°C. The internal capacity was aimed to be 200cc for the sufficiently continuous use. Structures to be connected to or assembled with peripheral parts such as a mounting arm and a port were also determined. All the requirements for the oil catch tank are listed in Table 3. Subsequently, the design strategy was discussed considering the high design flexibility of the L-PBF process. As a result, it was decided to adopt a monolithic structure without any fastenings and welds whereas conventional tanks consist of multiple components as exemplified in Figure 1. A monolithic structure is expected to lead to a drastic weight reduction because of not only the absence of fasteners but the omission of screw hole or welding also allows for a thinner wall design. Based on the requirements and the design strategy, a conceptual structure was established as described in Figure 14. The design has the monolithic hollow structure with the walls of 0.5mm thick which is obviously difficult, or even impossible to fabricate through classical processes. In turn, a Mises stress distribution on the conceptual design was investigated by the FEM analysis under the conditions listed in Table 4. The result in Figure 15 displays that the stresses over the

minimum yield strength at 150°C obtained in this study, 249MPa, are induced extensively, which indicates that a deformation of the tank potentially takes place during usage. Moreover, this geometry has an issue from viewpoint of the printing process. There are small radii on the corners of the vessel part and the bases of the mounting arms and the ports. The L-PBF process brings a complex thermal history to the material because of the dynamic and high energy input. Thus, some thermal stresses and residual stresses during printing will always occur in any cases and can be amplified by the small radius, leading to a part failure or deformation.

Table 3 Design requirements

Durability	Pressure resistance	Internal pressure of 1.5MPa at 150°C
	Vibration resistance	40G at 150°C
Structure	Inner capacity	200cc
	Quantity of port	5
	Quantity of mounting arm	3

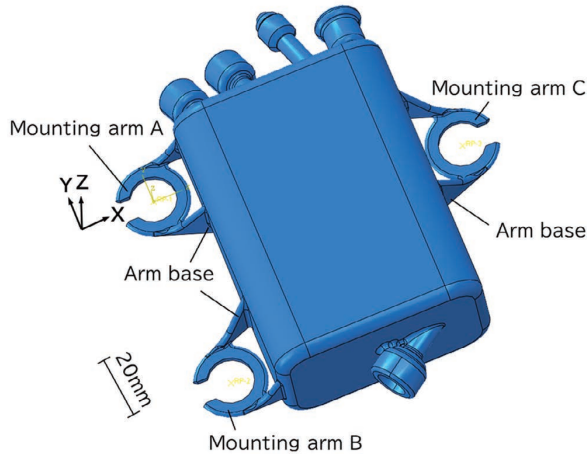


Fig. 14 Conceptual design

Table 4 FEM analysis conditions

Material Characteristic	Young's modulus	64.4GPa
	Poisson's ratio	0.33
Boundary condition	Mounting arm A	Completely fixed
	Mounting arm B	Fixed along Y and Z axis
	Mounting arm C	Fixed along X and Z axis
Load	Internal pressure	1.5MPa
	Vibrational acceleration	40G along Z axis

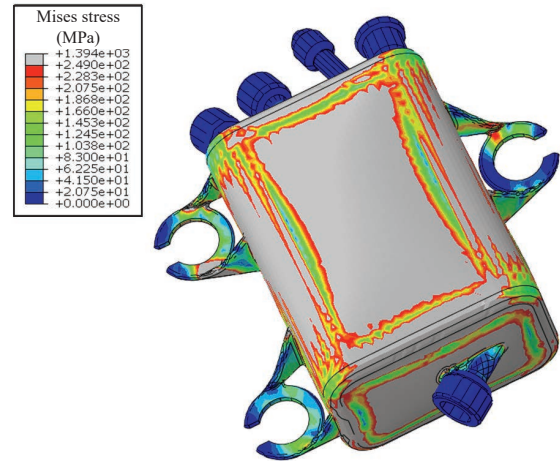


Fig. 15 Mises stress distribution on conceptual design

Hence, the design was modified so that the stresses associated with both the actual usage and the printing process can be lower. As a consequence, the updated design for the tank has become a more rounded outline as described in Figure 16. The rounded shape relieves the high stress at the edges and the sharp corners. It should be noted that the wall thicknesses have been tailored varying from location to location according to the induced stress distribution. Owing to the design flexibility of the L-PBF process, there is no need to make the walls thicker uniformly, instead, appropriate amount of material is supplemented as needed in the area where it is required. The shapes of the ports have been also changed for ease of assembly. The FEM analysis was again carried out and has revealed all the induced stresses are lower than the material yield strength as described in Figure 17. Interestingly, the stresses induced around the mounting arms have also decreased remarkably even though the geometries around them have hardly changed. The following mechanism is considered to reduce the stresses around the mounting arms. Before the design modification, the induced internal pressure causes a large deformation on the vessel part together with the displacement of all the mounting arm bases. Based on the analysis conditions shown in Table 4, despite the displacement of the bases, the mounting arms are not allowed to move freely. This can generate large stresses especially for completely fixed mounting arm A. Thus, reinforcing the vessel part can reduce displacement of the bases, which can consequently decrease the stresses around the mounting arms as well.

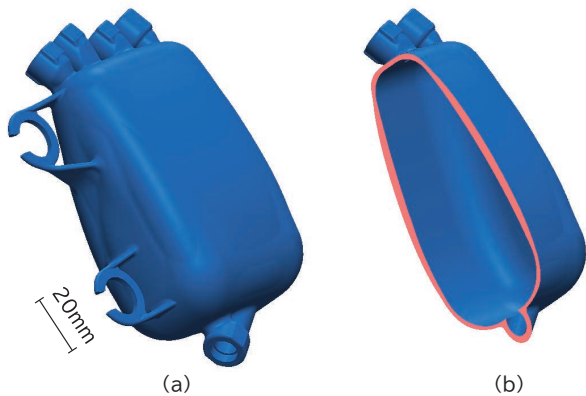


Fig. 16 (a) Appearance and (b) cross-sectional view of redesigned tank

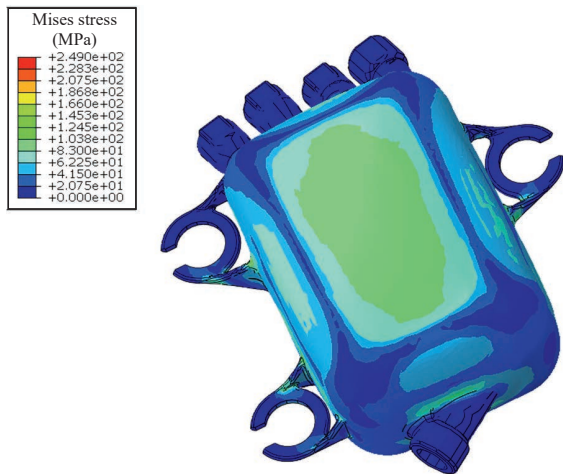


Fig. 17 Mises stress distribution on redesigned tank

The modified Goodman diagram is utilized to validate the reliability from the perspective of fatigue behavior. The minimum tensile strength at 150°C (340MPa), the minimum yield strength at 150°C (249MPa) and the fatigue strength of the 45°-orientated specimen (51MPa) are used to draw the diagram. Relatively high mean principal stresses  $\sigma_m$  and stress amplitudes  $\sigma_a$  on several locations are detected by the FEM analysis as shown in Figure 18. These values are then plotted in the modified Goodman diagram as shown in Figure 19. This diagram shows all the plotted points are below the line given by the modified Goodman relation, which suggests this tank could withstand the prescribed fatigue stress. To evaluate the contribution of the redesign to the weight reduction, the weight of the redesigned tank has been compared to that of a conventionally manufactured tank comprising multiple components. The conventional tanks have an

estimated weight of 295g. On the other hand, the weight of the redesigned tank in this work is calculated to be 110g, which is 63% lighter than a conventionally designed one.

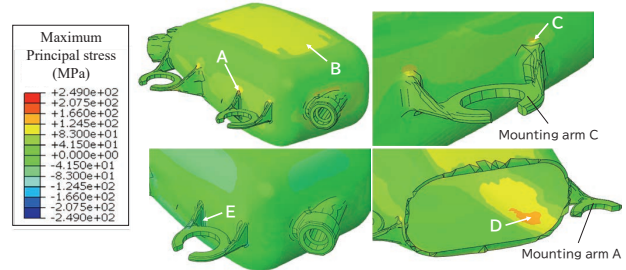


Fig. 18 Principal stress distribution on redesigned tank

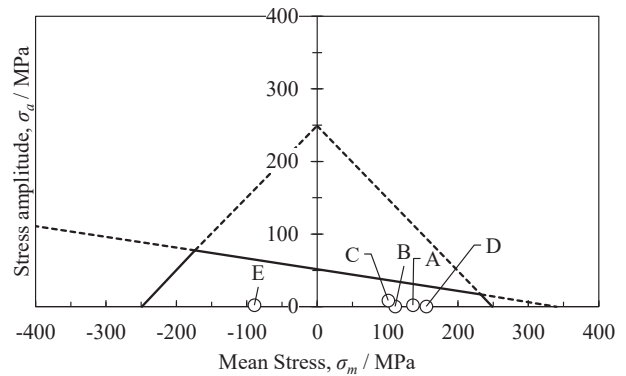


Fig. 19 Modified Goodman diagram with plots of analyzed stress

### 3-4. Experimental validation of newly designed tank

A fabrication of the redesigned tank was conducted with the same printing parameters as when the test specimens were produced. In fact, the rounded outline in the redesigned tank has a negative effect on the support structure design. The challenge is that, inside the rounded vessel part, there are always downward facing surfaces almost parallel to the building platform regardless of the part orientation. As it is well known, the L-PBF process basically needs support structures underneath the downfacing surfaces having an angle smaller than a critical angle to prevent the surfaces from warping or collapsing during building. However, internal support structures must be avoided since it cannot be removed afterward. Therefore, the printing parameters for the internal surfaces with the angle lower than 45° were slightly modified in order to build with no support

structures. Specifically, they were printed under a lower energy density condition. As a result, the redesigned tank was successfully fabricated as shown in Figure 20. X-ray computed tomography (X-ray CT) was carried out using FF35 CT with the voltage of 150kV and the current of 70μA, which can provide images with 70μm voxel size. The result shows no visible defects as shown in Figure 21. A piece taken from the vessel part of the fabricated tank was used for a Vickers hardness test and a chemical composition analysis with inductively coupled plasma atomic emission spectrometry (ICP-AES) and spectrophotometry. The averaged hardness was 172.0 HV5, which almost corresponds to that of the test coupon. On the other hand, the composition of the fabricated tank differs from that of powder, particularly for Mg as shown in Table 5. This can be attributed to the high energy input to the powder bed during the laser irradiation. According to the previous studies<sup>[23][24]</sup>, the FEM analyses have indicated that the melt pool temperature of Al alloys momentarily reaches up to around 2,000°C. Such an extremely high temperature could encourage evaporation of volatile elements including Mg. Kimura et al. also reported Mg depletion in Al-Si-Mg alloy fabricated by the L-PBF process<sup>[25]</sup>. Although it is difficult to quantitatively evaluate the influence of the decrease in Mg on the mechanical properties, this phenomenon should be taken into careful consideration because Mg, as a solid solution strengthening and precipitation strengthening element, is a key element to enhance the mechanical properties of Al alloys.



Fig. 20 Appearance of fabricated tank



Fig. 21 Transparent image by X-ray CT

Table 5 Chemical composition variation before and after fabrication

	Mg	Sc	Zr	Mn	Si	Fe	Al
Powder	4.90	0.78	0.29	0.41	0.06	0.17	Bal.
Fabricated tank	3.79	0.80	0.27	0.40	0.02	0.16	Bal.
Variation	-1.11	0.02	-0.02	-0.01	-0.04	-0.01	—

The pressure resistance of the redesigned 3D-printed tank was investigated by the method sketched in Figure 22. The tank was filled with perfluoropolyether fluorinated fluid as the pressure medium and placed in a furnace heated to 150°C. 4 of the 5 ports were plugged for sealing and the another was connected to a pressure source through an intensifier. The pressure was increased statically from ambient to 1.5MPa and then held for 4 hours. As a result, the test was completed with no mechanical failure of the tank. After that, the geometry change due to the pressure resistance test was evaluated by an optical CMM (Coordinate Measuring Machine) -scanner, MetraSCAN750 Elite as shown in Figure 23. Only very slight deformation less than 0.15mm was observed, indicating the tank is sufficiently resistant to the prescribed pressure and temperature.

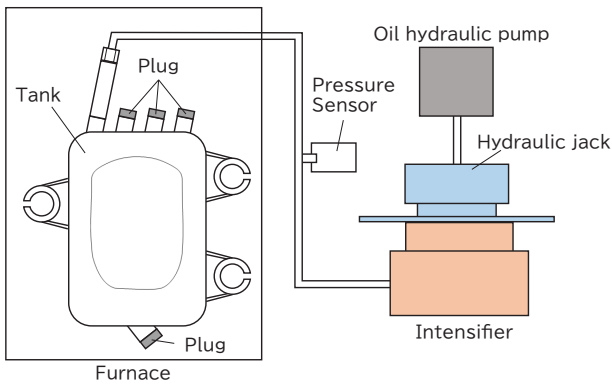


Fig. 22 Schematic diagram of pressure resistance test

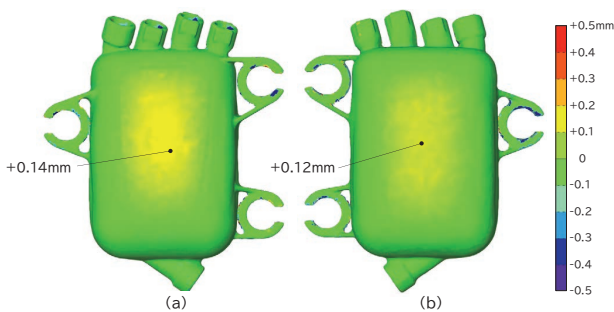


Fig. 23 Deformation of front and back side after pressure resistance test

## 4 CONCLUSIONS

This work attempted to develop the lightweight oil catch tank for the PVS using the Al-Mg-Sc alloy and the L-PBF technique, and which has led following conclusions.

- (1) The Al-Mg-Sc alloy fabricated by the L-PBF process exhibited the tensile characteristics superior to the wrought high-strength Al alloy, which can be attributed to the distinct metallurgical features such as extremely refined grains, uniformly dispersed fine precipitates.
- (2) The printing parameters were optimized to produce the highly dense part with no evident defects.
- (3) The lightweight design has been created considering the design flexibility of the L-PBF process and the material strength. The design has the monolithic hollow structure with varying the wall thickness from location to location, which cannot be produced by conventional processes.

- (4) By further parameter adjustment based on the optimal conditions, the lightweight tank was successfully produced with no internal support structures despite the downward facing surfaces almost parallel to the building platform.
- (5) The fabricated tank was demonstrated to have the prescribed pressure resistance.

## REFERENCES

- [1] Gregory, Guinther. and Scott, Smith., "Formation of Intake Valve Deposits in Gasoline Direct Injection Engines," SAE Int. J. Fuels Lubr. 9(3), 2016, doi:10.4271/2016-01-2252.
- [2] Shinya, Sano., Takahisa, Yashiro., Keiji, Takizawa., and Tatsuhiko, Mizutani., "Development of New Motor for Compact-Class Hybrid Vehicles," EVS International Battery, Hybrid and Fuel Cell Electric Symposium – Abstract, 2016
- [3] Dirk, Herzog., Vanessa, Seyda., Eric, Wycisk., and Claus, Emmelmann., "Additive manufacturing of metals," Acta Materialia 117, 371-392, 2016 doi:10.1016/j.actamat.2016.07.019.
- [4] William, E. Frazier., "Metal Additive Manufacturing: A Review," Journal of Materials Engineering and Performance 23(6), 1917-1928, 2014, doi:10.1007/s11665-014-0958-z.
- [5] Ming, Tang., P. Chris, Pistorius., Sneha, Narra., and Jack, L. Beuth., "Rapid Solidification: Selective Laser Melting of AlSi10Mg," JOM Vol. 68, No. 3, 960-996, 2016, doi:10.1007/s11837-015-1763-3.
- [6] Mitsuru, Adachi. and Shuuzi, Koizumi., "Present State of Metal Additive Manufacturing Promoting Revolution of Manufacturing and Issues for Practical Application," J. JFS Vol. 91, No. 9, 603-611, 2019, doi:10.11279/jfes.91.603.
- [7] Wengang, Zhai., Wei, Zhou., Zhiguang, Zhu. and Sharon Mui Ling, Nai., "Selective Laser Melting of 304L and 316L Stainless Steels: A Comparative Study of Microstructures and Mechanical Properties," steel research int., 93, 2100664, 2022, doi:10.1002/srin.202100664.
- [8] Nesma, T. Aboulkhair., Ian, Maskery., Chris, Tuck., Ian, Ashcroft. et al., "The microstructure and mechanical properties of selectively laser melted AlSi10Mg: The effect of a conventional T6-like heat treatment," Materials

- Science & Engineering A667, 139-146, 2016, doi:10.1016/j.msea.2016.04.092.
- [9] Shunyu, Liu. and Yung C., Shin., "Additive manufacturing of Ti6Al4V alloy: A review," *Materials and Design* 164, 107552, 2019, doi:10.1016/j.matdes.2018.107552.
- [10] Carla, Gonçalves Machado., Mélanie, Despeisse., Mats, Winroth. and Elias, Hans Dener Ribeiro da Silva., "Additive manufacturing from the sustainability perspective: proposal for a self-assessment tool," *Procedia CIRP* 81, 482-487, 2019, doi:10.1016/j.procir.2019.03.123.
- [11] Lore, Thijs., Frederik, Verhaeghe., Tom, Craeght., Jan, Van Humbeeck. et al. "A study of the microstructural evolution during selective laser melting," *Acta Materialia* 58, 3303-3312, 2010, doi:10.1016/j.actamat.2010.02.004.
- [12] A.F, Norman., P.B, Prangnell. and R.S, Mcewen., "The solidification behaviour of dilute aluminium-scandium alloys," *Acta mater.* Vol. 46, No. 16, 5715-5732, 1998.
- [13] V.G, Davydov., T.D, Rostova., V.V, Zakharov., Yu.A, Filatov. et al., "Scientific principles of making an alloying addition of scandium to aluminium alloys," *Material Science and Engineering A280*, 30-36, 2000.
- [14] Shingo, Iwamura. and Yasuhiro, Miura., "STEM-EDS analysis of the composite Al<sub>3</sub>(Sc,Zr) precipitates in an Al-Sc-Zr alloy" *Journal of Japan Institute of Light Metals*, Vol. 56, No. 2, 100-104, 2006.
- [15] A.B, Spierings., K, Dawson., T, Heeling., P.J, Uggowitzer. et al., "Microstructural features of Sc- and Zr-modified Al-Mg alloys processed by selective laser melting," *Materials and Design* 115, 52-63, 2017, doi:10.1016/j.matdes.2016.11.040.
- [16] A.B, Spierings., K, Dawson., P.J, Uggowitze. and K, Wegener., "Influence of SLM scan-speed on microstructure, precipitation of Al<sub>3</sub>Sc particles and mechanical properties in Sc- and Zr-modified Al-Mg alloys," *Material and Design* 140, 134-143, 2018, doi:10.1016/j.matdes.2017.11.053.
- [17] Takahiro, Kimura., Takayuki, Nakamoto., Tomoatsu, Ozaki., Takao, Miki. et al., "Microstructures and aging characteristics of Al-Mg-Sc alloy fabricated by selective laser melting," *Journal of The Japan Institute of Light Metals*, Vol. 70, No. 10, 467-474, 2020, doi:10.2464/jilm.70.567.
- [18] Yunjia, Shi., Kun, Yang., Shravan, K. Kairy., Frank, Palm. et al., "Effect of platform temperature on the porosity, microstructure and mechanical properties of an Al-Mg-Sc-Zr alloy fabricated by selective laser melting," *Material Science & Engineering A* 732, 41-52, 2018, doi:10.1016/j.msea.2018.06.049.
- [19] Eric, A. Jäggle., Zhendong, Sheng., Liang, Wu., Lin, Lu. et al., "Precipitation Reaction in Age-Hardenable Alloys During Laser Additive Manufacturing," *JOM*, Vol. 68, No. 3, 943-949, 2016, doi:10.1007/s11837-015-1764-2.
- [20] S, Kumar. and K.A.Q, O'Reilly., "Influence of Al grain structure on Fe bearing intermetallics during DC casting of an Al-Mg-Si alloy," *Materials Characterization* 120, 311-322, 2016, doi:10.1016/j.matchar.2016.09.017.
- [21] The Aluminum Association., "Aluminum standards and data (2003)."
- [22] Nesma, T. Aboulkhair., Ian, Maskery., Chris, Tuck., Ian, Ashcroft. et al., "Improving the fatigue behavior of a selectively laser aluminium alloy: Influence of heat treatment and surface quality," *Materials and Design* 104, 174-182, 2016, doi:10.1016/j.matdes.2016.05.041.
- [23] Shiwen, Liu., Junjie, Zhu., Haihong, Zhu., Jie, Yui. et al., "Effect of the track length and track number on the evolution of the molten pool characteristics of SLMed Al alloy: Numerical and experimental study," *Optics and Laser Technology* 123, 105924, 2020, doi:10.1016/j.optlastec.2019.105924.
- [24] Zhonghua, Li., Bao-Qiang, Li., Peikang, Bai., Bin, Liu. et al., "Research on the Thermal Behaviour of a Selectively Laser Melted Aluminium Alloy: Simulation and Experiment," *Materials* 11, 1172, 2018, doi:10.3390/ma11071172.
- [25] Takahiro, Kimura., Takayuki, Nakamoto., Tomoatsu, Ozaki., Kazuki, Sugita. et al., "Microstructural formation and characterization mechanism of selective laser melted Al-Si-Mg alloys with increasing magnesium content," *Materials Science & Engineering A* 754, 786-298, 2019, doi:10.1016/j.msea.2019.02.015.

■ 著者



**渡邊 慧太**  
Keita Watanabe  
生産技術本部  
材料技術部



**栗田 洋敬**  
Hirotaka Kurita  
生産技術本部  
材料技術部



**岩崎 進也**  
Shinya Iwasaki  
生産技術本部  
材料技術部



**三井 理功**  
Riku Mitsui  
PF 車両開発統括部  
SV 開発部

**長尾 隆史**  
Takashi Nagao  
日本軽金属株式会社  
グループ技術センター

**田代 継治**  
Tsuguharu Tashiro  
日本軽金属株式会社  
グループ技術センター

**市村 誠**  
Makoto Ichimura  
株式会社松浦機械製作所  
技術本部

**加納 佳明**  
Yoshiaki Kano  
株式会社松浦機械製作所  
技術本部

**楠井 潤**  
Jun Kusui  
東洋アルミニウム株式会社  
顧問